Optimizing Acquisition Times for Total-Body Positron-Emission Tomography/Computed Tomography with Half-Dose ^{18}F-Fluorodeoxyglucose in Oncology Patients

Yibo He
Department of nuclear medicine, Zhongshan hospital, Fudan university
Yushen Gu
Department of nuclear medicine, Zhongshan hospital, Fudan university
Haojun Yu
Department of nuclear medicine, Zhongshan hospital, Fudan university
Bing Wu
Department of nuclear medicine, Zhongshan hospital, Fudan university
Siyang Wang
Department of nuclear medicine, Zhongshan hospital, Fudan university
Hui Tan
Department of nuclear medicine, Zhongshan hospital, Fudan university
Yanyan Cao
Department of nuclear medicine, Zhongshan hospital, Fudan university
Shuguang Chen
Department of nuclear medicine, Zhongshan hospital, Fudan university
Xiuli Sui
Department of nuclear medicine, Zhongshan hospital, Fudan university
Yiqiu Zhang
Department of nuclear medicine, Zhongshan hospital, Fudan university
Hongcheng Shi (shi.hongcheng@zs-hospital.sh.cn)
Department of nuclear medicine,zhongshan hospital,Fudan university

Research Article

Keywords: Half-dose, Protocol optimization, Total-body PET/CT, Image quality, Lesion detectability

Posted Date: December 14th, 2021

DOI: https://doi.org/10.21203/rs.3.rs-1144588/v1

Abstract

Purpose

The present study aimed to explore the boundary of acquisition time and propose an optimized acquisition time for total-body positron emission tomography (PET)/computed tomography (CT) oncological imaging using half-dose ^{18}F-fluorodeoxyglucose (FDG) activity based on clinical diagnostic needs.

Methods

In this retrospective study, an exploration cohort (October 2019 to December 2019) of 46 oncology patients was first studied. The acquisition time for all patients was 15 min and the acquired images were reconstructed and further split into 15-, 8-, 5-, 3-, 2, 1-min duration groups (abbreviated as G15, G8, G5, G3, G2, and G1). The image quality and lesion detectability of reconstructed PET images with different acquisition times were evaluated subjectively (5-point scale, lesion-detection rate) and objectively (standardized uptake values, target-to-background ratio). In the same way, the filtered protocols were further validated in a cohort of 147 oncology patients (December 2019 to June 2021).

Results

In the exploration dataset, the subjective scores for G1, G2, G3, G5, and G8 were 2.0 ± 0.2, 2.8 ± 0.3, 3.1 ± 0.2, 3.9 ± 0.3, and 4.1 ± 0.2, respectively. Two cases in G1 were rated as 1 point. No significant difference in scores was observed between G5 and G8 (p = 0.89). In general, groups with a longer acquisition time showed lower background uptake and lesion conspicuity. Compared with G15, lesion-detection rate significantly reduced to 85.3% in G1. In the validation dataset, the subjective score was 2.9 ± 0.2 for G2, 3.0 ± 0.0 for G3, 3.5 ± 0.4 for G5, 4.0 ± 0.2 for G8, and 4.5 ± 0.4 for Gs. Only the scores between G2 and G3 were not significantly different (p > 0.99). The detection rates (204 lesions) significantly reduced to 94.1-89.7% in G3 and G2 (all p < 0.001).

Conclusion

A 2-min acquisition protocol provided acceptable performance in certain groups and specific medical situations. And protocols with acquisition times ≥ 5 min could provide comparable lesion detectability as regular protocols, showing better compatibility and feasibility with clinical practice.

Introduction

As a non-invasive medical imaging modality, positron-emission tomography/computed tomography (PET/CT) plays a crucial role in cancer diagnosis, staging, restaging, and efficacy assessments. Currently,

the most widely available PET/CT tracer is the ^{18}F-labelled glucose analogue fluorodeoxyglucose (FDG) [1]. In routine clinical practice, only a small amount (≤1%) of the radiation emitted by the tracer injected into the patient's body is detected during PET/CT due to the limited field of view (FOV) and the attenuation or scattering of a large portion of the photon pairs within the FOV [2]. Thus, high-quality PET images are generated either by increasing the injected dose of the tracer or by prolonging the acquisition time, both of which may result in health-and-safety consequences for patients.

Many researchers [3–5] have attempted to improve the photon-detection rate of PET. In 2019, a total-body PET/CT scanner with a 194-cm-long axial FOV was introduced. This scanner was designed to have a superior sensitivity of 176 kcps/MBq and a high spatial resolution of 2.9 mm, and can theoretically, provide an approximately 40-fold sensitivity gain over other conventional PET scanners used for total-body imaging [6]. The improved sensitivity provides feasible opportunities for low-dose imaging or short-acquisition protocols.

Tan et al. demonstrated that total-body PET with half-dose ^{18}F-FDG activity and an acquisition time of 2 min could achieve a comparable image quality to conventional PET in lung cancer [7]. However, this result could not be directly extrapolated to other tumors, and a universally accepted acquisition protocol has not yet been developed. A recent study [8] recommended a total acquisition time of 5 min as the regular acquisition protocol for full-dose (3.7 MBq/kg) total-body PET imaging. Therefore, it is logical to presume that a 10-min acquisition time would be sufficient as the routine acquisition protocol for total-body PET imaging with half-dose FDG. In this study, we aimed to identify a suitable acquisition protocol for half-dose total-body PET oncological imaging by analyzing several acquisition times and the quality of the resultant PET images.

Materials And Methods

Patient selection

This retrospective study included two cohorts of patients: the initial exploration cohort and the clinical validation cohort. The initial exploration cohort consisted of 46 consecutive patients who underwent ^{18}F-FDG total-body PET/CT with half-dose activity for oncological diagnosis and/or clinical staging in our department (from October to December 2019). This cohort was used to establish the preliminary optimization scheme of acquisition time. The second cohort included 147 patients (from December 2019 to June 2021) with malignancy or suspected malignancy who were selected retrospectively in an attempt to not only confirm the results of the first cohort but also to further identify the optimal range of acquisition times.

The inclusion and exclusion criteria were the same for both cohorts. The key inclusion criteria were patients with definite pathological diagnoses from a surgical specimen who were untreated before surgery. In addition, contrast-enhanced CT or contrast-enhanced magnetic resonance imaging was performed before surgery to rule out false-negative findings on PET images. The exclusion criteria were

as follows: (1) relative preoperative treatments or no authentic pathological evidence, (2) diffuse lesions in the liver, (3) lesion biopsy with negative results, and (4) claustrophobia or other conditions causing poor cooperation. The study was approved by the institutional review board of Zhongshan Hospital, Fudan University, and informed consent was acquired from all enrolled patients.

PET/CT examination

All patients fasted for at least 6 h before the administration of a half dose of ^{18}F-FDG, with a fluctuation of 20% (mean dose: exploration cohort, 1.88 ± 0.09 MBq/kg; validation cohort, 1.88 ± 0.10 MBq/kg). In the exploration cohort, raw images of all patients were obtained over a total acquisition time of 15 min on a 194-cm-long axial FOV total-body PET/CT scanner (uEXPLORER, United Imaging Healthcare, Shanghai, China) with the 3D list-mode. All PET images during the 15-min period were reconstructed, and then, the images were split into the 8-, 5-, 3-, 2-, and 1-min acquisition groups to mimic fast-acquisition scenarios. For brevity, the image series reconstructed with acquisition times of 15 to 1 min are abbreviated as G15, G8, G5, G3, G2, and G1. In the clinical validation cohort, data acquisition was performed for 15 or 10 min in the 3D list-mode. The images obtained using the 15- and 10-min acquisition times are collectively referred to as Gs images. The reason for grouping these two types of images together is that in April 2020, the standard acquisition time in our department was set at 10 min for optimization purposes. To further explore the results of the exploration cohort, all PET images were reconstructed and further divided into Gs, G8, G5, G3, and G2 images.

All PET images were reconstructed using an ordered subset expectation maximization algorithm that incorporated high-resolution time-of-flight and point-spread function modelling, with a spectrum of parameters: 3 iterations; 20 subsets; matrix, 192 × 192; slice thickness, 1.443 mm; and FOV, 600 mm (voxel size, 3.125 × 3.125 × 1.443 mm^3) with a Gaussian post-filter (3 mm). The acquisition parameters for diagnostic CT were as follows: tube current modulation; voltage, 120 kV; pitch, 0.9625; and reconstructed slice thickness, 1 mm with a slice increment of 1 mm. All image analysis was conducted using a commercial medical image-processing workstation (uWS-MI, United Imaging Healthcare, Shanghai, China).

Qualitative image analysis in both cohorts

To identify an acceptable threshold of acquisition time, we performed a qualitative analysis of the reconstructed PET images from the exploration cohort. Before starting the assessments, two nuclear medicine physicians (Z.Y.Q. and T.H., with 11 and 2 years of experience in interpreting oncological ^{18}F-FDG PET/CT images, respectively) were given the criteria for image grading. They jointly assessed 10 test cases by means of a 5-point Likert scale, as used in previous studies [9, 10]. After familiarizing themselves with the scoring method, the observers independently analyzed the image quality of the PET scans. Both readers were blinded to the medical history of each patient, injected dose, and acquisition time of the PET images. The order of image presentation was randomized to reduce the bias. The scoring of the images on the Likert scale was mainly based on the overall impression of the image quality, which was categorized as follows: 5 points, excellent image quality; 4 points, superior to the average image

quality in routine practice in our department; 3 points, equal to the quality used in clinical practice, 2 = acceptable image quality with no need to rescan, and 1 = non-diagnostic image requiring rescanning (Fig. 1). Subsequently, under the same dose regimen, the proposed acquisition duration was further validated in the clinical validation cohort. The subjective image quality in this cohort was rated independently using the same scoring criteria by the same qualified physicians. Inter-reader agreement analyses were performed in each cohort.

Quantitative image analysis in the exploration cohort

The objective image-quality measurements were conducted by an experienced technician under the supervision of a nuclear medicine physician. For measuring the background liver uptake, a two-dimensional circular ROI with a diameter of 20 mm was manually placed in the right lobe of liver at the section of the portal vein bifurcation, avoiding all distinguishable lesions and intrahepatic large blood vessels. For measuring the background uptake of the mediastinal blood pool, the same size ROI or an appropriately reduced ROI was plotted in the descending aorta at the level of the bronchial bifurcation, avoiding the vascular wall. Semi-quantitative uptake parameters of the liver and mediastinal blood pool, the SUV_{max}, the mean standardized uptake value (SUV_{mean}), and the SD of the ROI were measured and documented. All the same-size ROIs were simultaneously drawn on the same slice and site to minimize inter-site variation between all groups.

As representative indices of objective image quality as well as lesion conspicuity, the SUV_{max} and SUV_{peak} of the lesions and the TBR were included in the final analysis. The SUV_{max} and SUV_{peak} of the lesions were measured by manually drawing a volume of interest on the slice with the maximum lesion diameter on transverse view. The TBR, which refers to lesion contrast, was calculated as the SUV_{peak} of the lesion divided by the SUV_{mean} of the liver.

Lesion detectability

The lesion-detection rates for all groups of images were calculated to quantify the lesion detectability of the PET images from the two cohorts. The number of lesions identified in the G15 (exploration dataset) and Gs (validation dataset) images were selected as references. For each cohort, all PET images were read during a joint session by the same two nuclear medicine physicians, after an interval of 2 weeks since the qualitative analysis. The whole process of reading was in line with the principle of blinding and randomization to minimize any potential memory effect. Information of all ^{18}F-FDG-avid lesions confidentially identified by the readers was documented and selected for the analysis. Images with poor quality or excessive background noise that made the lesion contrast unfavorable were marked. Discrepancies in lesion identification were resolved via mutual consultation.

Statistical analysis

Statistical analysis and graph generation were conducted using SPSS 26.0 (IBM, SPSS) and Prism 8 (GraphPad Software Inc.), with p values < 0.05 being considered significant. Continuous variables were reported as mean ± SD. The weighted Cohen kappa test was used to determine the inter-rater agreement

of the subjective scores. The strength of the agreement was graded as slight (0.00 to 0.20), fair (0.21 to 0.40), moderate (0.41 to 0.60), substantial (0.61 to 0.80), and excellent (0.81 to 1.00). Differences in the subjective image scores between image groups were assessed using the Kruskal-Wallis rank-sum test with the Dunn post-hoc test. To minimize the influence of inter-patient differences, repeated-measures one-way analysis of variance was used to determine whether there were significant differences in quantitative parameters among the groups. Differences in lesion-detection rate were evaluated using the chi-square test.

Results

Patient cohorts

The present study involved two patient cohorts: an initial exploration cohort for the analysis of different acquisition times and a clinical validation cohort for the validation of the initial results and the optimization of acquisition times. The results for these two cohorts are presented below.

Initial exploration cohort

Patient characteristics

The demographic and clinical data of the patients are summarized in Table 1. We enrolled a total of 46 patients (34 men, 12 women) in the exploration cohort, with a mean age of 61.5 ± 8.8 years, a mean body mass index (BMI) of 24.1 ± 3.5 kg/m^2, and a mean injected FDG dose of 1.88 ± 0.09 MBq/kg. The overall distribution of primary neoplasms in this cohort was as follows: lung neoplasms, 19 patients; colorectal cancer, 17 patients; liver cancer, 4 patients; biliary tract cancer, 2 patients; and stomach neoplasms, 4 patients. Lymph node metastases were suspected in 18 patients, while distant metastases were not present in any patient. The distribution of the primary tumors and lymph node lesions is shown in detail in Table 2.

Evaluation of image quality

Qualitative (subjective) image analyses were performed by two readers, and their findings showed excellent inter-rater agreement, with a weighted kappa of 0.848 (95% confidence interval [CI]: 0.800–0.897). The average qualitative scores for images with acquisition times of 1, 2, 3, 5, and 8 min (henceforth referred to as G1, G2, G3, G5, and G8, respectively) were 2.0 ± 0.2, 2.8 ± 0.3, 3.1 ± 0.2, 3.9 ± 0.3, and 4.1 ± 0.2, respectively (Table 3). Even for the G1 images, the average score indicated visually acceptable images with no need for rescanning. In the case of two patients, however, the G1 images were given a score of 1 point by both readers. The subjective scores of the G5 and G8 images were significantly higher than those of the other images (all $p < 0.05$). No significant difference in subjective scores was observed between the G5 and G8 images ($p = 0.89$). In addition, no distinct difference was identified between the G2 and G3 images ($p > 0.99$).

The results of the objective image-quality assessments are presented in Table 4. We calculated the average difference in the objective quality of the G1, G2, G3, G5, and G8 images from that of the G15 images (15-min acquisition time; Fig. 2) by subtracting the measurement results of G1, G2, G3, G5, and G8 by those of the G15 images (referred to as 1-15, 2-15, 3-15, 5-15, and 8-15 for the sake of simplicity). In general, images with longer acquisition times showed lower standardized uptake values (SUVs). The maximum SUV (SUV_{max}) of the liver was significantly lower in the G15 and G8 images than in the other images (all $p < 0.05$), but did not differ between the G15 and G8 images ($p > 0.99$). The SUV_{max} of the mediastinal blood pool was significantly lower in the G15, G8, and G5 images than in the G3, G2, and G1 (all $p < 0.05$), but did not differ between the G15 and G8 images ($p = 0.13$) or between the G8 and G5 images ($p = 0.92$). The average standard deviation (SD) of the regions of interest (ROIs) in the liver and mediastinal blood pool significantly differed between the G15 images and the other images (all $p \leq 0.001$). The trend of the between-group differences in average SUVs was similar to the trend observed in the SUVs. Moreover, these differences were statistically significant among all groups (all $p < 0.05$), except for the differences in the blood pool SUVmax ($p = 0.61$) and SUV_{SD} ($p = 0.09$) between the 8-15 and 5-15 groups.

Lesion detectability

Pathological examination confirmed a total of 75 lesions in the 46 patients in the exploration cohort. Of these, 7 lesions in 6 patients (2 liver lesions, 1 lung lesion, and 4 lymph node lesions) were not recognizable on G15 images. In all, 47 primary lesions and 21 suspicious lymph node metastases were detected on G15 images. With the G15 data as the reference, the lesion-detection rates were 85.3% (58/68) and 97.1% (66/68) for the G1 and G2 images, respectively, and 100% (68/68) for the remaining images. On the G1 images, 10 lesions from 6 patients were not identifiable, including 1 lesion in the liver and 9 lesions in the lymph nodes. The lesion-detection rate significantly differed between the G15 and G1 images ($p = 0.001$).

For the assessment of lesion conspicuity, a total of 56 out of 75 lesions were pathologically positive and included for analysis. The SUV_{max}, SUV_{peak}, and target-to-background ratio (TBR) of these 56 lesions were significantly lower on G15 images than on the remaining images (all $p \leq 0.04$); moreover, these values did not significantly differ among the remaining images (all $p \geq 0.08$; Table 5).

Clinical validation cohort

Patient characteristics

A total of 147 eligible patients (79 men, 68 women) with a mean age of 59.4 ± 12.1 years, mean body weight of 63.8 ± 11.7 kg, mean BMI of 23.6 ± 3.6 kg/m^2, and mean injected FDG dose of 1.88 ± 0.10 MBq/kg were included in this dataset (Table 1). After integrating the pathological data, we included 240 lesions in the final analysis: 163 primary tumors, 69 suspicious lymph node metastases, and 8 distant metastases. Three patients had multiple primary tumors: one patient had small intestine cancer with

schwannomas; one had bladder cancer with ureteral cancer, and another patient had liver cancer with gastrointestinal stromal tumor. Distant metastases were present in 4 patients, including 3 patients with colorectal cancer and liver metastasis, and 1 patient with breast cancer and bone metastasis. The distribution of all pathologically confirmed lesions in the validation cohort is shown in detail in Table 6.

Subjective image quality

The weighted kappa coefficient between the readers was 0.760 (95% CI: 0.723–0.797), which indicated a substantial degree of agreement. The subjective scores for the G2, G3, G5, G8, and Gs (acquisition time, 10 or 15 min) images were 2.9 ± 0.2, 3.0 ± 0.0, 3.5 ± 0.4, 4.0 ± 0.2, and 4.5 ± 0.4, respectively (Table 3). The scores for the G2 and G3 images were approximately 3 points or slightly lower than 3 points. Significant differences in these scores were observed between any two groups (all $p < 0.05$), except for G2 and G3 ($p > 0.99$).

Lesion detectability

Of the 240 lesions, 36 lesions were not clearly identified on Gs images: 11 liver lesions, 5 biliary tract lesions, 2 pancreatic lesions, 2 bladder lesions, 1 gallbladder lesion, and 15 lymph node lesions. Compared to the Gs images, the G2, G3, G5, and G8 images had lesion-detection rates of 89.7% (183/204), 94.1% (192/204), 99.0% (202/204), and 100% (204/204), respectively. The distribution of the 21 lesions that went undetected on G2 images was as follows: biliary tract (n = 4), liver (n = 2), pancreas (n = 1), stomach (n = 1), bladder (n = 1), small intestine (n = 1), lymph nodes (n = 10), and liver metastasis (n = 1). The distribution of lesions that were unidentifiable on G3 images was as follows: biliary tract (n = 2), bladder (n = 1), liver (n = 1), and lymph nodes (n = 8). The lesion-detection rates for the G5 and G8 images were not significantly lower than the rates for the Gs images (all $p \geq 0.50$).

Discussion

The predicted 40-fold gain in sensitivity of the total-body PET compared to conventional PET scans would offer a wide range of combinations of injection doses and scan times, providing the foundations for the creation of scans with credible image quality based on clinical needs and the need for different acquisition speeds, which was the theoretical basis of this study.

At a constant injected dose, a higher image quality always requires a longer acquisition time [11]. To determine the acceptable threshold of acquisition time at half-dose FDG, we conducted a preliminary exploration study. The results indicated that the subjective quality scores of the G1, G2, and G3 images were significantly inferior to those of the G5 and G8 images (all $p < 0.05$). Nevertheless, the subjective quality scores of G1 (2.0 ± 0.2) and G2 (2.8 ± 0.3) images were acceptable, though these images provided limited clinical information. Only reconstructed PET images with acquisition times of 3 min or longer received subjective scores that are defined as appropriate for routine clinical application in our department (mean scores for G3, G5, and G8 images: 3.1 ± 0.2, 3.9 ± 0.3, and 4.1 ± 0.2, respectively). Notably, for 2 patients, the G1 images received a score of only 1 point each, which indicated that the

images were non-diagnostic, and the patients had to be rescanned. The objective quality analysis showed that the SUVs of the liver and mediastinal blood pool gradually decreased with increase in the acquisition time, in the order of G1, G2, G3, G5, G8, and G15; this is consistent with the results reported by Zhang et al. [9]. This finding suggested that the extension of acquisition time could reduce image noise and permit further reduction in the SUVs of the liver and mediastinal blood pool, thereby enhancing the image contrast [12]. Additionally, with the G15 images as the reference, the lesion-detection rate was 100% for all images, except for the G1 (85.3%, $p = 0.001$) and G2 (97.1%, $p = 0.50$) images. A drawback of the short acquisition protocol is an increase in noise caused by low photon counts, which ultimately results in false-positive lesions on visual PET image assessment. Thus, some of the positive lesions identified using short acquisition protocols possibly represent false-positive lesions, as was typical for the G1 images (Fig. 3). However, we did not observe any differences in the lesion-detection rates of the G3, G5, and G8 images, possibly due to the small sample size and selection bias. Although the shortened acquisition time had a positive impact on the SUVs and TBRs of the lesions in the exploration cohort, its tendency to result in impaired image quality and indistinguishable false-positive lesions indicate the need for a further optimized acquisition protocol.

Our preliminary results were further validated in a dataset with a larger sample size. The subjective image-quality analysis in the validation dataset indicated that the scores for the G2 and G3 images (2.9 ± 0.2 *vs.* 3.0 ± 0.0; $p > 0.99$) were significantly lower than those for the other images (all $p < 0.05$). The subjective G2 and G3 scores were only 3 points or slightly lower than 3 points, which is the minimum score required for routine clinical practice in our department. We speculated that one reason for the impaired image quality in some patients was the BMI (up to 36.0 kg/m^2). PET image quality is influenced by several factors, including BMI [13–16], which were not strictly controlled for in the patients enrolled in our study. Thus, this patient group was, to some extent, a reflection of the real clinical situation. Compared to the Gs images, the G8 and G5 images showed lesion-detection rates of 100% and 99.0%, respectively, while the G3 and G2 images showed significantly lower lesion-detection rates (94.1% and 89.7%, respectively; all $p < 0.001$). These findings are consistent with those of previous phantom and clinical studies [9, 17]. Thus, we concluded that a protocol with an acquisition time of 5 min or longer could provide comparable lesion detectability as the regular protocol. This result also reflected the differences between G2 or G3 and G5 or G8, providing a new perspective for the rational assessment of the SUVs and TBRs of the lesions in the exploration cohort. Unlike the G2 and G3 scans, the G5 and G8 images exhibited a high degree of lesion conspicuity without a significant compromise in image quality (Fig. 4). Nevertheless, it should be noted that some lesions were still missed at an acquisition time of 5 min, such as hilar cholangiocarcinoma (HC). Although HC is a highly malignant tumor where FDG theoretically tends to accumulate, liver uptake is often not significantly lower than the tumor uptake in most clinical cases. Lee et al. have reported a low cut-off SUV_{max} of 3.65 for differentiating HC from benign tumors [18]. This result might give some hints about individualizing the acquisition time appropriately for certain hypometabolic tumors in clinical practice.

On the basis of the results from the two cohorts, we propose a 5–8 min acquisition protocol as an optimized universal scheme for the clinical application of total-body PET/CT at half-dose FDG, which is within the recommended range (3–10 min) proposed by Sui et al. [19]. Indeed, our study showed a gradient of acquisition times for different clinical needs. An acquisition time of 2 min was sufficient to obtain clinically acceptable image quality, while acquisition times of 3–5 min were adequate for most clinical applications (e.g., gastrointestinal neoplasms). In some cases, particularly for the liver, a 5–8-min protocol was preferable to obtain more reliable information for disease assessment. It is worth noting that an acquisition time of 8 min not only resulted in high image quality but also served as an alternative to the 10-min protocol in terms of lesion detectability. The 2-min acquisition protocol we identified and validated was required for some specific occasions for two reasons. The first reason is that this protocol has a reasonably low radiation dose, which helps to decrease radiation exposure from medical procedures for patients and medical staff. The European Association of Nuclear Medicine guidelines recommend a minimum acceptable administered dose of 7 MBq·min·bed^{-1}·kg^{-1} (with a PET bed overlap of >30%) for ^{18}F-FDG PET/CT oncological examination in adults [1]. Zhang et al. reported a dose of 4.67 MBq·min·kg^{-1} for a 60-s acquisition protocol at full dose, which was already lower than the recommended minimum acceptable dose [9]. In this study, we further lowered the “minimum threshold” to 3.76 MBq·min·kg^{-1} after multiplication by 2 min at half-dose. This reduction will enable the performance of low-dose PET imaging for numerous applications in vulnerable groups (e.g., pregnant women) and patients requiring repeat PET examinations [20]. The second reason for the 2-min acquisition protocol was that the total scan time was significantly reduced. For a standard “skull to mid-thighs” whole-body tumor-imaging protocol at full-dose FDG, the PET acquisition takes about 10–20 min for the body part and approximately 3 min for the head [21]. In contrast, the present study showed that half-dose total-body PET/CT can be performed using an acquisition time of only 2 min in just one bed position; this protocol is recommended for patients with unstable physical conditions, as it would greatly improve patient comfort.

Our study had several limitations. First, a selection bias might exist because only patients with diagnoses confirmed by postoperative pathology were included in our study. Second, as this was a single-center retrospective study, the results should be externally validated in a larger multicenter trial to further reduce selection bias. Third, the lesion-detection rate is affected by the size, shape, volume, and surroundings of the lesion as well as the readers’ experience. These intriguing factors warrant further investigation. Finally, based on our experience, we used a fixed reconstruction algorithm and parameters for all reconstructed PET images. In the future, the application of new reconstruction algorithms and optimized parameters may provide better image quality in short-duration scanning.

In conclusion, total-body PET/CT with half-dose FDG in oncology patients allows for a significant reduction in acquisition time with comparable image quality and lesion detectability to the regular acquisition protocol. A 2-min acquisition, though somewhat lowering quality, provided acceptable performance and warrants consideration in certain groups and specific medical situations. However, a 5- to 8-min acquisition protocol demonstrates better compatibility and feasibility with clinical practice, providing sufficient information to meet the needs of clinical diagnosis.

Declarations

Funding This study is supported by Science and Technology Committee of Shanghai Municipality (20DZ2201800), Clinical Research Project of Zhongshan Hospital, Fudan University (2020ZSLC63), Shanghai "Rising Stars of Medical Talent" Youth Development Program (SHWRS[2020]_087), Clinical Research Plan of SHDC (No. SHDC2020CR3079B), Shanghai Municipal Key Clinical Specialty (shslczdzk03401), and Shanghai Municipal Commission of Economy and Informatization (201901014).

Competing Interests The authors have no relevant financial or non-financial interests to disclose.

Author contributions Yibo He and Yushen Gu were involved in the study design and manuscript preparation. Yiqiu Zhang and Hui Tan contributed to image interpretation. Bing Wu and Siyang Wang helped with data analyses. Yanyan Cao and Xiuli Sui conducted data collection and processing. Haojun Yu and Shuguang Chen helped with image acquisition and reconstructions. Hongcheng Shi and Yiqiu Zhang designed the study and contributed to editing and reviewing the manuscript. All authors discussed the results and approved the final manuscript.

Data Availability The data that support the findings of this study are available from the corresponding author upon reasonable request.

Ethics approval All procedures performed in studies involving human participants were in accordance with the ethical standards of the institutional and/or national research committee and with the 1964 Helsinki declaration and its later amendments or comparable ethical standards.

Consent to participate Written informed consent was obtained from all individual participants included in the study.

Consent to publish The authors affirm that human research participants provided informed consent for publication of the studied data and the images.

References

1. Boellaard R, Delgado-Bolton R, Oyen WJ, et al. FDG PET/CT: EANM procedure guidelines for tumour imaging: version 2.0. Eur J Nucl Med Mol Imaging. 2015;42(2):328–54.
2. Cherry SR, Jones T, Karp JS, Qi J, Moses WW, Badawi RD. Total-Body PET: Maximizing Sensitivity to Create New Opportunities for Clinical Research and Patient Care. J Nucl Med. 2018;59(1):3–12.
3. Poon JK, Dahlbom ML, Moses WW, et al. Optimal whole-body PET scanner configurations for different volumes of LSO scintillator: a simulation study. Phys Med Biol. 2012;57(13):4077–94.
4. Surti S, Karp JS. Impact of detector design on imaging performance of a long axial field-of-view, whole-body PET scanner. Phys Med Biol. 2015;60(13):5343–58.
5. Schmall JP, Karp JS, Werner M, Surti S. Parallax error in long-axial field-of-view PET scanners-a simulation study. Phys Med Biol. 2016;61(14):5443–55.

6. Spencer BA, Berg E, Schmall JP, et al. Performance Evaluation of the uEXPLORER Total-Body PET/CT Scanner Based on NEMA NU 2-2018 with Additional Tests to Characterize PET Scanners with a Long Axial Field of View. J Nucl Med. 2021;62(6):861–70.
7. Tan H, Sui X, Yin H, et al. Total-body PET/CT using half-dose FDG and compared with conventional PET/CT using full-dose FDG in lung cancer. Eur J Nucl Med Mol Imaging. 2021;48(6):1966–75.
8. Hu P, Zhang Y, Yu H, et al. Total-body 18F-FDG PET/CT scan in oncology patients: how fast could it be. Eur J Nucl Med Mol Imaging. 2021;48(8):2384–94.
9. Zhang YQ, Hu PC, Wu RZ, et al. The image quality, lesion detectability, and acquisition time of 18F-FDG total-body PET/CT in oncological patients. Eur J Nucl Med Mol Imaging. 2020;47(11):2507–15.
10. Sonni I, Baratto L, Park S, et al. Initial experience with a SiPM-based PET/CT scanner: influence of acquisition time on image quality. EJNMMI Phys. 2018;5(1):9.
11. Akamatsu G, Ishikawa K, Mitsumoto K, et al. Improvement in PET/CT image quality with a combination of point-spread function and time-of-flight in relation to reconstruction parameters. J Nucl Med. 2012;53(11):1716–22.
12. Halpern BS, Dahlbom M, Quon A, et al. Impact of patient weight and emission scan duration on PET/CT image quality and lesion detectability. J Nucl Med. 2004;45(5):797–801.
13. Büsing KA, Schönberg SO, Brade J, Wasser K. Impact of blood glucose, diabetes, insulin, and obesity on standardized uptake values in tumors and healthy organs on 18F-FDG PET/CT. Nucl Med Biol. 2013;40(2):206–13.
14. Cook GJ, Wegner EA, Fogelman I. Pitfalls and artifacts in 18FDG PET and PET/CT oncologic imaging. Semin Nucl Med. 2004;34(2):122–33.
15. de Groot EH, Post N, Boellaard R, Wagenaar NR, Willemsen AT, van Dalen JA. Optimized dose regimen for whole-body FDG-PET imaging. EJNMMI Res. 2013;3(1):63.
16. Sánchez-Jurado R, Devis M, Sanz R, Aguilar JE, del Puig Cózar M, Ferrer-Rebolleda J. Whole-body PET/CT studies with lowered ^{18}F-FDG doses: the influence of body mass index in dose reduction. J Nucl Med Technol. 2014;42(1):62–7.
17. Matheoud R, Leva L, Secco C, et al. Small lesions detectability with the Biograph 16 Hi-Rez PET/CT scanner and fast imaging protocols: performance evaluation using an anthropomorphic thoracic phantom and ROC analyses. Ann Nucl Med. 2011;25(3):179–88.
18. Lee SW, Kim HJ, Park JH, et al. Clinical usefulness of 18F-FDG PET-CT for patients with gallbladder cancer and cholangiocarcinoma. J Gastroenterol. 2010;45(5):560–66.
19. Sui X, Liu G, Hu P, et al. Total-Body PET/Computed Tomography Highlights in Clinical Practice: Experiences from Zhongshan Hospital, Fudan University. PET Clin. 2021;16(1):9–14.
20. Liu G, Hu P, Yu H, et al. Ultra-low-activity total-body dynamic PET imaging allows equal performance to full-activity PET imaging for investigating kinetic metrics of 18F-FDG in healthy volunteers. Eur J Nucl Med Mol Imaging. 2021;48(8):2373–83.
21. Vandenberghe S, Moskal P, Karp JS. State of the art in total body PET. EJNMMI Phys. 2020;7(1):35.

Tables

Table 1
Characteristics of the patients in the exploration and validation cohorts

Patient characteristic	Initial exploration cohort (n = 46)	Clinical validation cohort (n = 147)
Gender (male/female)	34*/12*	79*/68*
Age (years)	61.5 ± 8.8 [43-81]	59.4 ± 12.1 [20-87]
Weight (kg)	67.0 ± 11.2 [46.3-90.7]	63.8 ± 11.7 [38.3-105.0]
Height (cm)	166.4 ± 7.4 [152.6-184.4]	164.3 ± 8.7 [139.0-185.2]
Blood glucose	5.7 ± 1.1 [4.1-9.1]	5.9 ± 1.4 [3.7-10.8]
BMI (kg/m^2)	24.1 ± 3.5 [17.4-33.1]	23.6 ± 3.6 [15.5-36.0]
Injected dose (MBq)	125.9 ± 21.1 [85.1-174.4]	119.7 ± 22.3 [73.1-216.0]
Injected dose per unit weight (MBq/kg)	1.88 ± 0.09 [1.73-2.15]	1.88 ± 0.10 [1.67-2.18]
Waiting time (min)	64.7 ± 17.2 [40-106]	73.4 ± 17.5 [40-115]
Lesion counts (lesion/patient)	1.6 ± 0.8 [1–4]	1.6 ± 1.1 [1–8]
Lesion short diameter (mm)	15.8 ± 12.8 [4.9-85.5]	20.8 ± 18.6 [4.0-120.4]
Note.— Unless otherwise specified, data are presented as mean ± SD [range: min to max].		
* Data are numbers of patients. BMI = body mass index.		

Table 2
Pathological distribution of tumors in the exploration cohort

Pathological tumor type	Primary tumor (n = 46)				Lymph node metastasis (n = 18)			
	N1	N2	N3	Total	N1	N2	N3	Total
Lung (n = 19)	17	1	1	22*	2	0	0	2*
Biliary tract (n = 2)	2	0	0	2*	1	1	0	3*
Liver (n = 4)	3	1	0	5*	0	1	0	2*
Colorectum (n = 17)	17	0	0	17*	8	3	1	17*
Stomach (n = 4)	4	0	0	4*	1	0	0	1*
Total	43	2	1	50*	12	5	1	25*

Note.— Unless otherwise indicated, data are numbers of patients.

* Data are numbers of lesions.

N1, N2, and N3 indicate the number of patients with 1, 2, and 3 lesions, respectively.

Table 3
Qualitative image analysis in the exploration and validation cohorts

Group	Rater	Excellent (score 5)	Good (score 4)	Average (score 3)	Acceptable (score 2)	Non-diagnostic (score 1)	Average score
Exploration cohort							
G1 (n=46)	Z.Y.Q.	0	0	3 (6.5%)	41 (89.2%)	2 (4.3%)	2.0 ± 0.2*
	T.H.	0	0	0	44 (95.7%)	2 (4.3%)	
G2 (n=46)	Z.Y.Q.	0	0	38 (82.6%)	8 (17.4%)	0	2.8 ± 0.3*
	T.H.	0	0	40 (87.0%)	6 (13.0%)	0	
G3 (n=46)	Z.Y.Q.	0	5 (10.9%)	41 (89.1%)	0	0	3.1 ± 0.2*
	T.H.	0	0	46 (100%)	0	0	
G5 (n=46)	Z.Y.Q.	0	36 (78.3%)	10 (11.7%)	0	0	3.9 ± 0.3*
	T.H.	0	43 (93.5%)	3 (6.5%)	0	0	
G8 (n=46)	Z.Y.Q.	2 (4.3%)	44 (95.7%)	0	0	0	4.1 ± 0.2*
	T.H.	10 (11.7%)	36 (78.3%)	0	0	0	
Clinical validation cohort							
G2† (n=147)	Z.Y.Q.	0	0	133 (90.5%)	14 (9.5%)	0	2.9 ± 0.2*
	T.H.	0	0	143 (97.3%)	4 (2.7%)	0	

Note.— Unless otherwise indicated, data are numbers of patients, and data in parentheses are percentages.

* Data are mean ± standard deviation.

† Groups from the clinical validation cohort.

Group	Rater	Excellent (score 5)	Good (score 4)	Average (score 3)	Acceptable (score 2)	Non-diagnostic (score 1)	Average score
G3† (n=147)	Z.Y.Q.	0	0	147 (100%)	0	0	3.0 ± 0.0*
	T.H.	0	1 (0.7%)	146 (99.3%)	0	0	
G5† (n=147)	Z.Y.Q.	0	76 (51.7%)	71 (48.3%)	0	0	3.5 ± 0.4*
	T.H.	0	85 (57.8%)	62 (42.2%)	0	0	
G8† (n=147)	Z.Y.Q.	1 (0.7%)	138 (93.9%)	8 (5.4%)	0	0	4.0 ± 0.2*
	T.H.	8 (5.4%)	134 (91.2%)	5 (3.4%)	0	0	
Gs† (n=147)	Z.Y.Q.	78 (53.1%)	69 (46.9%)	0	0	0	4.5 ± 0.4*
	T.H.	63 (42.9%)	84 (57.1%)	0	0	0	

Note.— Unless otherwise indicated, data are numbers of patients, and data in parentheses are percentages.

* Data are mean ± standard deviation.

† Groups from the clinical validation cohort.

Table 4
Background SUV and SDs in the exploration cohort

Measurement	G15	G8	G5	G3	G2	G1
Liver SUV_{max}	3.00 ± 0.52	2.98 ± 0.47	3.09 ± 0.49	3.19 ± 0.50	3.28 ± 0.53	3.53 ± 0.60
Difference in liver SUV_{max} between groups†		-0.02 ± 0.15†	0.09 ± 0.19†	0.19 ± 0.19†	0.28 ± 0.18†	0.53 ± 0.31†
Liver SD	0.084 ± 0.063	0.124 ± 0.055	0.166 ± 0.070	0.198 ± 0.072	0.236 ± 0.074	0.317 ± 0.100
Difference in liver SD between groups†		0.040 ± 0.067†	0.082 ± 0.082†	0.114 ± 0.084†	0.152 ± 0.089†	0.233 ± 0.110†
Mediastinal SUV_{max}	2.27 ± 0.37	2.30 ± 0.37	2.33 ± 0.40	2.41 ± 0.43	2.49 ± 0.45	2.61 ± 0.50
Difference in mediastinal SUV_{max} between groups†		0.04 ± 0.10†	0.07 ± 0.12†	0.14 ± 0.16†	0.22 ± 0.21†	0.35 ± 0.27†
Mediastinal SD	0.118 ± 0.049	0.144 ± 0.047	0.154 ± 0.039	0.171 ± 0.045	0.196 ± 0.054	0.249 ± 0.083
Difference in mediastinal SD between groups†		0.026 ± 0.040†	0.036 ± 0.047†	0.053 ± 0.060†	0.078 ± 0.079†	0.131 ± 0.103†

Note.— Data are mean ± standard deviation.

† The mean ± SD listed under the columns G8, G5, G3, G2, and G1 are the differences in the SUV_{max} and SDs between these groups and the G15 group.

SUV = standardized uptake value, SD = standard deviation.

Table 5
SUVs and TBRs of the lesions in the exploration dataset (n = 56)

Measurement	G15	G8	G5	G3	G2	G1
Lesion SUV_{max}	9.99 [1.03; 39.10]	11.60 [1.10; 46.44]	11.68 [1.18; 45.68]	12.01 [1.18; 47.40]	12.06 [1.13; 49.54]	12.27 [1.18; 50.31]
Lung (n = 19)	8.65 [1.03; 25.80]	8.60 [1.16; 24.89]	8.57 [1.18; 24.14]	8.57 [1.18; 24.49]	8.58 [1.13; 23.41]	8.58 [1.18; 23.52]
Liver (n = 5)	5.52 [3.17; 9.85]	5.69 [3.14; 11.20]	5.79 [3.41; 10.79]	6.06 [3.54; 12.01]	6.53 [3.60; 12.33]	6.93 [3.87; 13.24]
Colorectum (n = 17)	16.04 [5.57; 39.10]	20.80 [7.91; 46.44]	20.95 [7.48; 45.68]	21.84 [7.42; 47.40]	21.73 [7.78; 49.54]	22.16 [6.66; 50.31]
Stomach (n = 4)	10.30 [2.19; 26.65]	12.54 [2.77; 33.34]	13.16 [3.15; 34.52]	13.42 [2.61; 34.23]	13.59 [2.69; 34.62]	13.75 [2.30; 34.89]
Biliary tract (n = 2)	10.33 [9.13; 11.53]	10.08 [8.54; 11.61]	10.20 [8.74; 11.66]	10.62 [9.05; 12.18]	11.22 [9.31; 13.13]	12.00 [10.10; 13.89]
Lymph nodes (n = 9)	3.68 [1.10; 7.25]	3.79 [1.10; 8.38]	3.68 [1.24; 8.49]	3.70 [1.33; 8.53]	3.73 [1.15; 8.58]	3.74 [1.24; 8.46]
Lesion SUV_{peak}	8.27 [0.90; 29.96]	9.01 [0.52; 34.70]	8.99 [0.52; 33.93]	9.01 [0.55; 34.85]	9.07 [0.54; 33.97]	8.98 [0.68; 34.57]
Lung (n = 19)	7.07 [0.97; 19.60]	7.02 [1.04; 18.98]	6.97 [1.04; 18.55]	6.96 [1.02; 18.71]	6.97 [0.94; 18.45]	6.89 [0.93; 18.41]
Liver (n = 5)	5.25 [3.02; 9.24]	5.22 [2.93; 9.71]	5.26 [3.12; 9.53]	5.37 [3.17; 10.07]	5.56 [3.16; 10.18]	5.70 [3.33; 10.33]
Colorectum (n = 17)	13.13 [4.59; 29.96]	15.49 [5.40; 34.70]	15.45 [5.10; 33.93]	15.59 [5.00; 34.85]	15.58 [5.26; 33.97]	15.42 [4.57; 34.57]
Stomach (n = 4)	8.62 [1.93; 21.45]	9.55 [2.06; 24.32]	9.79 [2.41; 24.41]	9.56 [1.88; 23.09]	9.91 [2.19; 24.49]	9.87 [1.88; 24.56]
Biliary tract (n = 2)	9.55 [8.47; 10.62]	9.29 [7.85; 10.72]	9.40 [7.98; 10.81]	9.48 [8.12; 10.84]	9.83 [8.37; 11.29]	10.14 [8.63; 11.64]
Lymph nodes (n = 9)	2.86 [0.90; 5.99]	2.76 [0.52; 5.78]	2.69 [0.52; 5.74]	2.59 [0.55; 5.89]	2.60 [0.54; 5.83]	2.42 [0.68; 5.52]
Lesion TBR_{peak}	3.01 [0.37; 11.61]	3.40 [0.23; 13.14]	3.37 [0.22; 13.00]	3.37 [0.25; 13.46]	3.38 [0.25; 12.54]	3.30 [0.29; 12.27]

Note.— Data are mean [range: min to max].

SUV = standardized uptake value, TBR = target-to-background ratio.

Measurement	G15	G8	G5	G3	G2	G1
Lung (n = 19)	2.56 [0.37; 7.34]	2.59 [0.40; 7.19]	2.56 [0.40; 7.14]	2.51 [0.38; 7.01]	2.49 [0.35; 6.91]	2.47 [0.37; 6.78]
Liver (n = 5)	1.57 [1.08; 2.72]	1.69 [1.18; 3.10]	1.68 [1.27; 2.90]	1.72 [1.33; 3.02]	1.78 [1.28; 3.20]	1.79 [1.33; 3.10]
Colorectum (n = 17)	5.04 [1.98; 11.61]	6.09 [2.58; 13.14]	6.06 [2.40; 13.00]	6.13 [2.32; 13.46]	6.10 [2.27; 12.54]	5.93 [1.97; 12.27]
Stomach (n = 4)	3.01 [0.76; 7.20]	3.50 [0.82; 8.69]	3.53 [0.95; 8.51]	3.45 [0.75; 8.07]	3.60 [0.87; 8.87]	3.39 [0.76; 8.13]
Biliary tract (n = 2)	2.86 [2.74; 2.98]	3.09 [2.86; 3.31]	3.04 [2.86; 3.22]	3.07 [2.83; 3.31]	3.25 [2.93; 3.57]	3.40 [2.79; 4.01]
Lymph nodes (n = 9)	0.98 [0.38; 1.78]	0.98 [0.23; 2.03]	0.95 [0.22; 2.02]	0.91 [0.25; 2.05]	0.92 [0.25; 1.99]	0.83 [0.29; 1.74]
Note.— Data are mean [range: min to max].						
SUV = standardized uptake value, TBR = target-to-background ratio.						

Table 6
Pathological distribution of tumors in the clinical validation cohort

Pathological distribution	Clinical validation (n = 147)		
	Primary tumor	Lymph node metastasis	Distant metastasis
Lung (n = 11)	11/0/0 (11†)	1/0/1 (4†)	—
Biliary tract (n = 30)	29/1/0 (31†)	11/4/0 (19†)	—
Liver (n = 19)	16/2/1 (23†)	2/1/0 (4†)	—
Colorectum (n = 10)	10/0/0 (10†)	3/3/2/1 (19†)	1/0/2 (7†)
Stomach (n = 4)	3/0/1 (6†)	2/0/0 (2†)	—
Pancreas (n = 26)	24/2/0 (28†)	5/0/0 (5†)	—
Gallbladder (n = 5)	5/0/0 (5†)	0/1/1 (5†)	—
Bladder (n = 7)	4/3/0 (10†)	—	—
Kidney (n = 4)	4/0/0 (4†)	—	—
Breast (n = 3)	3/0/0 (3†)	1/0/0 (1†)	1/0/0 (1†)
Ovary (n = 4)	3/1/0 (5†)	—	—
Small intestine (n = 9)	9/0/0 (9†)	2/0/0 (2†)	—
Esophagus (n = 2)	2/0/0 (2†)	—	—
Mediastinum (n = 3)	3/0/0 (3†)	—	—
Pharynx (n = 3)	3/0/0 (3†)	0/0/0/0/0/0/1 (7†)	—
Skin (n = 1)	1/0/0 (1†)	1/0/0 (1†)	—
Uterus (n = 1)	1/0/0 (1†)	—	—
Bones (n = 1)	1/0/0 (1†)	—	—
Carotid body (n = 1)	1/0/0 (1†)	—	—
Muscle (n = 1)	1/0/0 (1†)	—	—

Note.— Values separated by virgules (/) indicate the number of patients with 1/2/3/4/5/6/7 lesions.

† Data are numbers of lesions.

Pathological distribution	Clinical validation (n = 147)		
	Primary tumor	Lymph node metastasis	Distant metastasis
Retroperitoneum (n = 2)	2/0/0 (2†)	—	—
Total (n = 147)	160†	69†	8†
Note.— Values separated by virgules (/) indicate the number of patients with 1/2/3/4/5/6/7 lesions.			
† Data are numbers of lesions.			

Figures

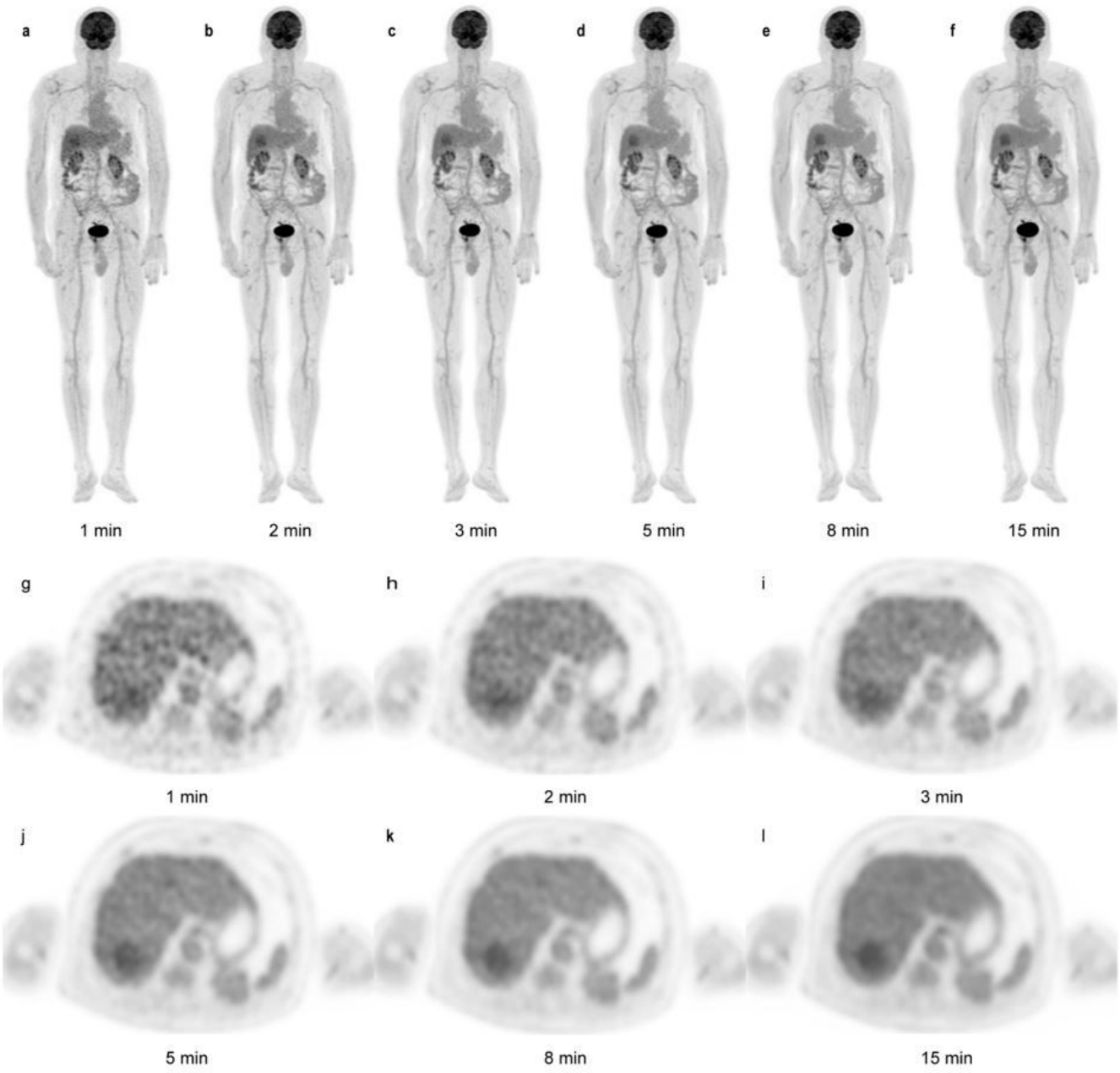

Figure 1

An example of qualitative analysis. An FDG-avid lesion with a diameter of 50.0 mm in the right posterior lobe of the liver is seen on G1 to G15 images with maximum intensity projection (MIP) (a–f) and the axial view (g–l). The axial-view G1, G2, G3, G8, and G15 images were given scores of 1, 2, 3, 4, and 5, respectively.

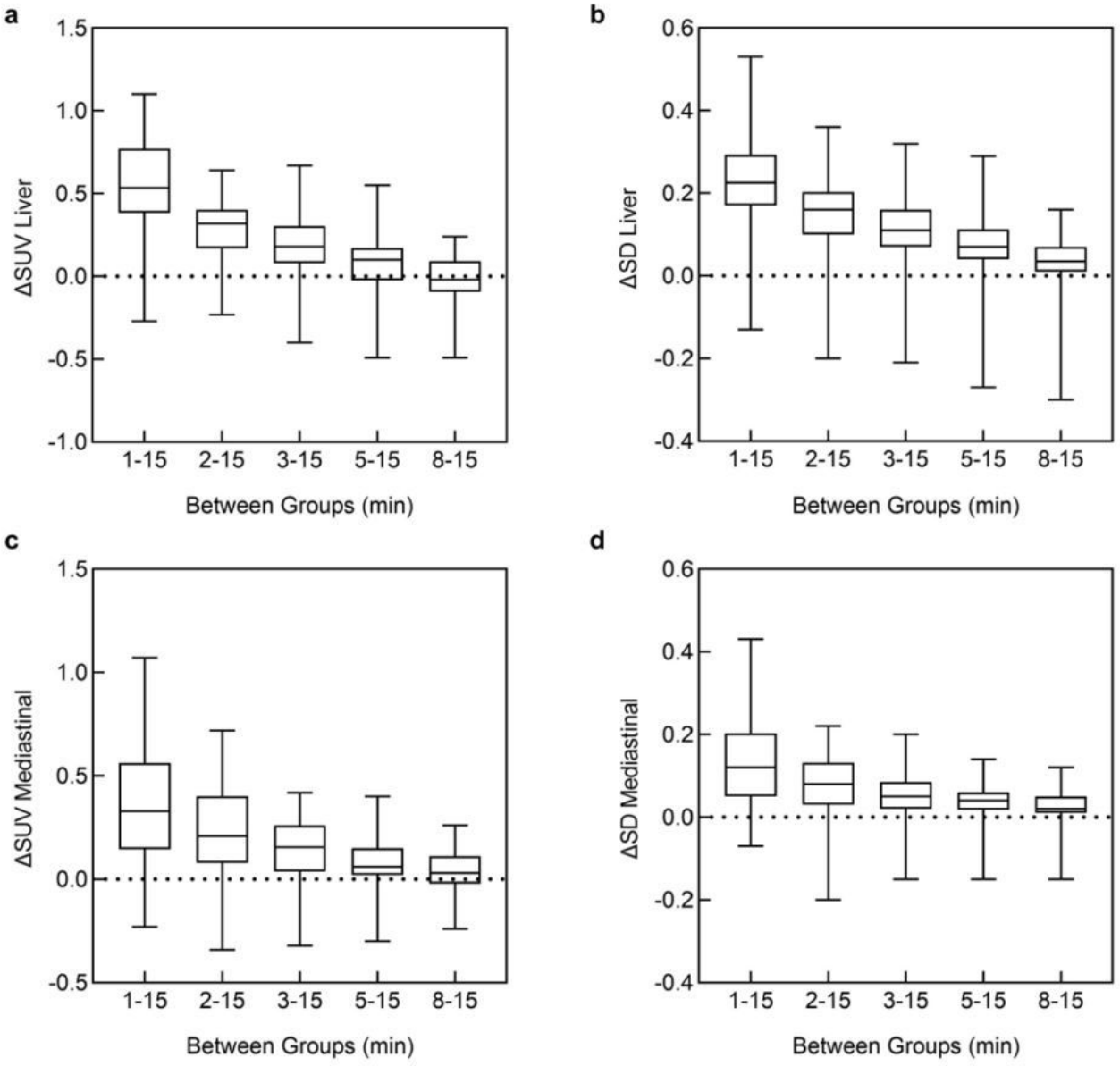

Figure 2

Box plots of the differences in liver and mediastinal SUVmax and SDs. The average difference of the G1, G2, G3, G5, and G8 images from the G15 images was calculated by subtracting the measurement results of G1, G2, G3, G5, and G8 by those of the G15 images (referred to as 1-15, 2-15, 3-15, 5-15, and 8-15 for simplicity). In general, the average difference decreased as the acquisition time increased. (a) The liver SUVmax was significantly lower on the G15 and G8 images than on the other short-duration images (all $p < 0.05$), but did not differ between the G15 and G8 images ($p > 0.99$). (b) The average SD in the liver significantly differed between the G15 images and all other images (all $p \leq 0.001$). (c) The mediastinal SUVmax was significantly lower on G15, G8, and G5 images than on G3, G2, and G1 images (all $p < 0.05$), but did not differ between the G15 and G8 images ($p = 0.13$) or between the G8 and G5 images ($p = 0.92$).

(d) The mediastinal SD significantly differed between the short-acquisition images and the G15 images (all $p < 0.05$).

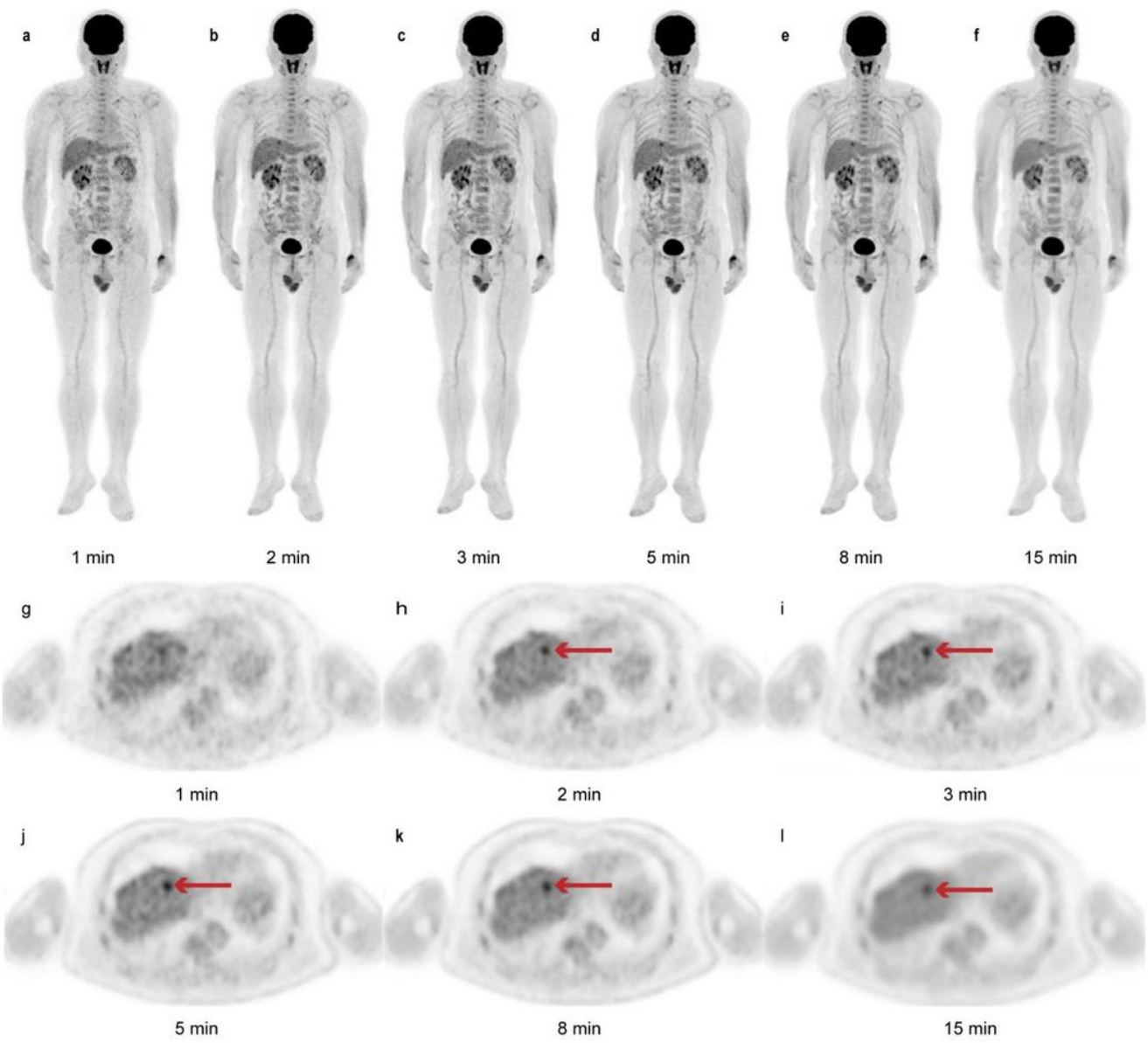

Figure 3

A 56-year-old man with intrahepatic cholangiocarcinoma. The images show a lesion on G1 to G15 images with maximum intensity projection (MIP) (a–f) and the axial view (g–l). As indicated by the red arrowheads, the lesion is clearly identified on the G2, G3, G5, G8, and G15 images, but cannot be distinguished from background noise when the acquisition time is reduced to 1 min (G1 images).

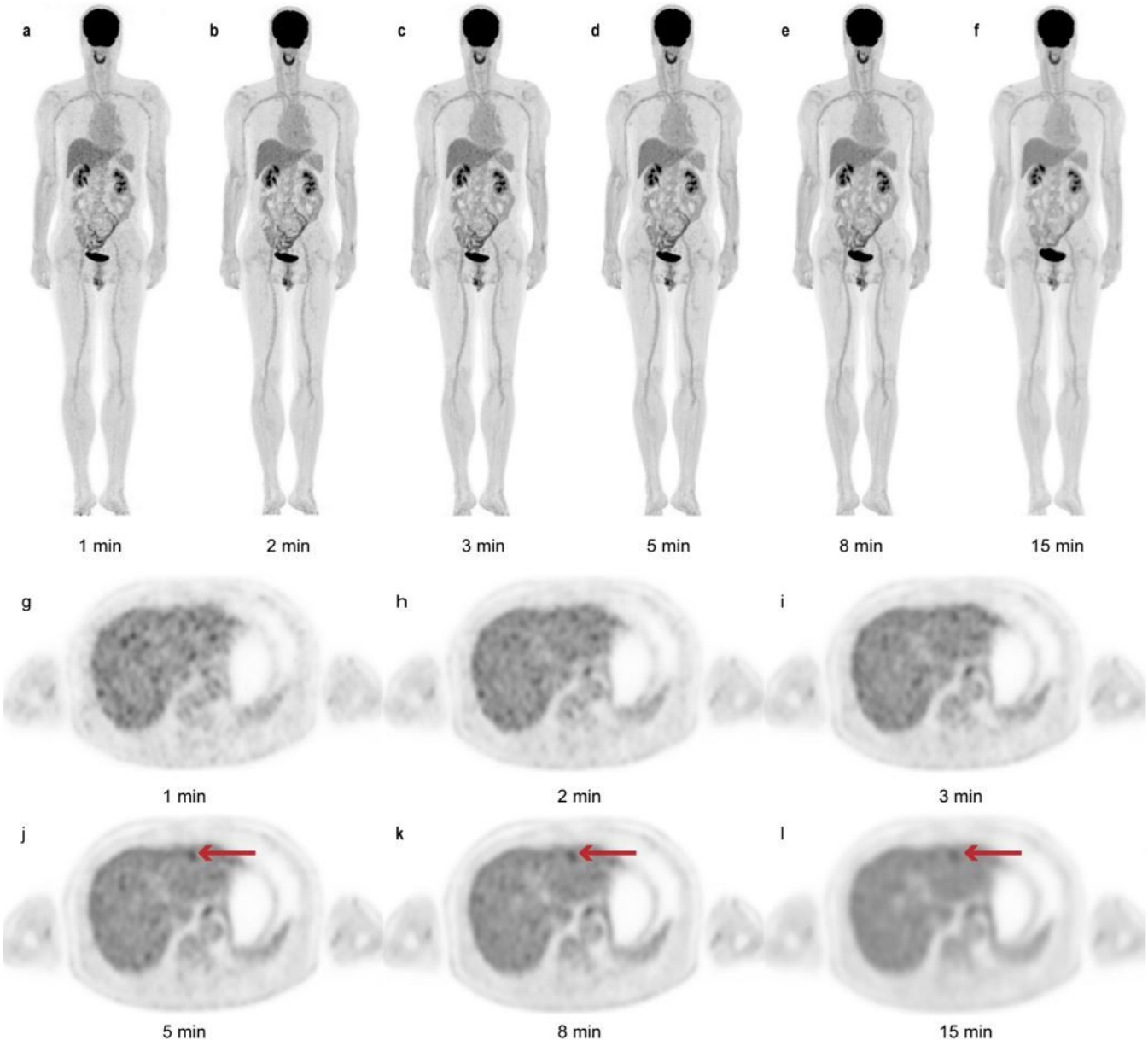

Figure 4

A 63-year-old man with hepatocellular carcinoma. The images show an FDG-uptake lesion in the left external lobe of the liver on G1 to G15 images with maximum intensity projection (MIP) (a–f) and the axial view (g–l). The background noise is notably higher on the G1, G2, and G3 images, which has resulted in impaired image quality and low confidence of lesion detectability. Thus, the lesion in the liver (arrows in j–l) was masked by the background noise when the acquisition time was 3 min or lower.